An Eigenfrequency Analysis of Mixed Rossby–Gravity Waves on Barotropic Vortices

WEI ZHONG

Key Laboratory of Mesoscale Severe Weather, Nanjing University, and Nanjing Institute of Mesoscale Meteorology, Nanjing, China

DA-LIN ZHANG

Department of Atmospheric and Oceanic Science, University of Maryland, College Park, College Park, Maryland

ABSTRACT

In this study, the linearized, f-plane, shallow-water equations are discretized into a matrix eigenvalue problem to examine the full spectrum of free waves on barotropic (monopolar and hollow) vortices. A typical wave spectrum for weak vortices shows a continuous range between zero and an advective frequency associated with vortex Rossby waves (VRWs) and two discrete ranges at both sides associated with inertio-gravity waves (IGWs). However, when the vortex intensity reaches a critical value, higher-frequency waves will be "red shifted" into the continuous spectrum, while low-frequency waves will be "violet shifted" into the discrete spectrum, leading to the emergence of mixed vortex Rossby–inertio-gravity waves (VRIGWs).

Results show significant (little) radial wavelike structures of perturbation variables for IGWs (VRWs) with greater (much smaller) divergence than vorticity and the hybrid IGW–VRW radial structures with equal amplitudes of vorticity and divergence for mixed VRIGWs. In addition, VRWs only occur within a critical radius at which the perturbation azimuthal velocity is discontinuous. As the azimuthal wavenumber increases, lower-frequency waves tend to exhibit more mixed-wave characteristics, whereas higher-frequency waves will be more of the IGW type. Two-dimensional wave solutions show rapid outward energy dispersion of IGWs and slower dispersion of VRWs and mixed VRIGWs in the core region. These solutions are shown to resemble the previous analytical solutions, except for certain structural differences caused by the critical radius. It is concluded that mixed VRIGWs should be common in the eyewall and spiral rainbands of intense tropical cyclones. Some different wave behaviors associated with the monopolar and hollow vortices are also discussed.

1. Introduction

Intense tropical cyclones (TCs) often develop polygonal eyewalls, double eyewalls, and spiral rainbands in the inner-core regions (e.g., Willoughby et al. 1982; Marks and Houze 1987; Liu et al. 1997). These features, superimposed on the mean rotational flow, play an important role in determining the structural and intensity changes of TCs (Black and Willoughby 1992; Lee and Bell 2007; Chen et al. 2011). Earlier views on the dynamics of these perturbation structures were based on the theory of internal inertio-gravity waves (IGWs) (e.g., Kurihara 1976; Willoughby 1978; Elsberry et al.

1987). One caveat with this theory is that these observed structures often propagate much slower than pure IGWs. Thus, more attention later has been shifted to the vortex Rossby wave (VRW) theory of Macdonald (1968) who drew an analogy between spiral rainbands and Rossby waves around a rotating sphere (e.g., Guinn and Schubert 1993; Montgomery and Kallenbach 1997, hereafter MK; Wang 2002). Recent observational and modeling studies have shown the presence of intense divergence and cyclonic vorticity in the eyewall and spiral rainbands (Jorgensen 1984; Liu et al. 1999; Hogsett and Zhang 2009). Obviously, the IGW and VRW theories, describing the respective divergent and rotational flows, cannot provide a complete description of wave dynamics in TCs.

Recently, Zhong et al. (2009, hereafter ZZL) developed a theory for azimuthally propagating mixed vortex Rossby–inertio-gravity waves (VRIGWs) that are similar

Corresponding author address: Dr. Da-Lin Zhang, Department of Atmospheric and Oceanic Science, University of Maryland, College Park, 2419 CSS BLDG, College Park, MD 20742-2425.
E-mail: dalin@atmos.umd.edu

in many characters to the equatorial mixed Rossby–gravity waves found by Matsuno (1966), one of which is the presence of both rotational and divergent flows, in contrast to nondivergent VRWs. By neglecting the advection of the mean height by perturbation radial flows in the linearized, f-plane, shallow-water equations and justifying the radial variation of the Bessel parameter based on a real-data cloud-resolving TC simulation, ZZL were able to obtain a form of the Bessel equation for an azimuthal harmonic oscillator in the cylindrical coordinates with the following cubic wave-frequency equation exhibiting the coexistence of IGWs, VRWs, and mixed VRIGWs:

$$\omega^3 - (m^2 - F_r\eta\Omega)\omega + nR_0T_r = 0, \qquad (1a)$$

where ω is the intrinsic frequency; the Froude number F_r is the squared ratio of the rotational speed to the phase speed of surface gravity waves; the vortex Rossby number R_0 is the ratio of the mean rotation to its radial gradient of vertical absolute vorticity η; T_r is the curvature of azimuthal flows; Ω is the angular velocity; and $m(n)$ is the percentage distance of each node, corresponding to the positive roots of nth-order Bessel function of the first kind, between the TC center and the boundary radius for a given azimuthal wavenumber (WN) n. Note that all the variables in Eq. (1a) are nondimensional (see ZZL for more details). An important result from ZZL is that the normal-mode characteristics of the three different waves are determined by the following discriminant parameter associated with Eq. (1a); that is,

$$Q = \frac{(m^2 - F_r\eta\Omega)^3}{27} - \frac{1}{4}n^2R_0^2T_r^2. \qquad (1b)$$

Using a real-data model-simulated TC vortex as the basic state, ZZL found that (i) when $Q > 0$, there exist two high-frequency oppositely propagating IGWs and a low-frequency VRW propagating against the mean flow; (ii) when $Q = 0$, there are only two intermediate-frequency waves exhibiting the characteristics of mixed VRIGW; and (iii) when $Q < 0$, there is a single real solution corresponding to a cyclonic-propagating low-frequency VRIGW and two complex conjugate solutions associated with dynamically unstable VRIGWs. Thus, it is clear from Eq. (1b) that the smaller m is, the more likely it is that mixed VRIGWs will occur.

Because the analytical solution in Eq. (1a) was obtained after applying the above-mentioned two simplifying procedures, it is desirable to examine to what extent the results of ZZL can be generalized. Furthermore, little is understood about the spectral characteristics

of mixed VRIGWs in relation to IGWs and VRWs as described by the linearized shallow-water equations. Thus, in this study, we will use the same dynamical framework as in ZZL, but without making any approximation, to study various classes of waves propagating in TC-like vortices, with more attention given to mixed VRIGWs. This will be done by invoking numerical solutions of the linearized shallow-water equations. Numerical solutions are also desirable because ZZL assumed nonzero Doppler-shifted frequency like other theoretical wave-motion studies in order to derive the analytical normal-mode solutions.

Montgomery and Lu (1997, hereafter ML) have also invoked numerical solutions of the linearized shallow-water equations to study the spectrum and structures of VRWs and IGWs propagating in TC-like vortices. In addition, they examined the nature of "balanced" and "unbalanced" flows dominated by the respective rotational and divergent components of barotropic vortices. The divergent flows account for the adjustment of the mass and wind fields, depending upon the time scale of the motions. Recent studies have revealed the presence of quasi-balanced flows in intense TCs and other mesoscale convective systems (Davis and Weisman 1994; Wang and Zhang 2003; Zhang and Kieu 2006; Zhong et al. 2008). This implies that both divergence and rotation are important in these weather systems. Zeng et al. (1990) studied the wave spectrum and eigenfunction of two-dimensional shallow-water equations under the influences of westerly wind shears and found that the wave spectrum can be easily separated into two classes in the presence of weak flows: low-frequency Rossby waves with a continuous spectrum and high-frequency IGWs with a discrete spectrum; continuous versus discrete spectra will be discussed in section 3a. However, the spectrum of IGWs could extend into the continuous spectrum and overlaps with Rossby wave spectrum in the presence of strong westerly flows. As a result, low-frequency IGWs would resemble in many aspects those of Rossby waves, including those typical characteristics of low-frequency waves (e.g., quasi-balanced features).

The objectives of this study are (i) to examine the spectral and propagation characteristics of mixed VRIGWs in relation to VRWs and IGWs in rapidly rotating TC-like vortices and (ii) to provide a more complete understanding of wave spectrum using a linearized, finite-differenced shallow-water equations model, the so-called shallow-water vortex perturbation analysis and simulation (SWVPAS), developed by Nolan et al. (2001, hereafter NMG). They are achieved by numerically solving the shallow-water normal-mode equations and then examining their wave spectrum distribution for

given TC-like vortices. A third objective is to compare the wave propagation characteristics from the numerical solutions to those from the mixed-wave theory of ZZL.

The next section shows discretized normal-mode shallow-water equations (i.e., SWVPAS), discusses two different vortices used for VRIGWs studies, and then presents their frequency–WN relations for different signs of Q. Section 3 performs an eigenfrequency analysis of mixed VRIGWs, VRWs, and IGWs in SWVPAS, following ML and Zeng et al. (1990). Section 4 shows the structures and evolution of each class of the waves on a monopolar vortex with SWVPAS, and then compares the numerical solutions of propagating waves on a TC-like vortex to the analytical solutions of ZZL.

2. Numerical model and basic states

Consider the propagation of small-amplitude gravitational oscillations in a rapidly rotating shallow-water system allowing for the coexistence of rotational and divergent flows. The simplest governing equations used to describe these wave motions are the linearized, f-plane, shallow-water equations in polar (r, λ) coordinates (ML; ZZL), which is also the basic framework of SWVPAS, given by

$$\left(\frac{\partial}{\partial t} + \overline{\Omega}\frac{\partial}{\partial \lambda}\right)u' - \tilde{f}v' + g\frac{\partial h'}{\partial r} = 0, \qquad (2a)$$

$$\left(\frac{\partial}{\partial t} + \overline{\Omega}\frac{\partial}{\partial \lambda}\right)v' + \overline{\eta}u' + g\frac{\partial h'}{r\partial \lambda} = 0, \qquad (2b)$$

$$\left(\frac{\partial}{\partial t} + \overline{\Omega}\frac{\partial}{\partial \lambda}\right)h' + \overline{H}D' + \kappa u'\frac{d\overline{H}}{dr} = 0, \qquad (2c)$$

where u' and v' are the radial and azimuthal perturbation velocity, respectively; h' and $\overline{H}$ are the perturbation height and the mean equivalent depth, respectively; $\overline{V}(r)$ is the mean azimuthal wind, and $\overline{\Omega}(r) = \overline{V}(r)/r$ is the mean angular velocity; $\tilde{f} = f + 2\overline{\Omega}$ is the modified Coriolis parameter (f) varying with radius; $\overline{\eta} = f + 2\overline{\Omega} + rd\overline{\Omega}/dr$ is the mean vertical absolute vorticity; $D' = \partial ru'/r\partial r + \partial v'/r\partial \lambda$ denotes the perturbation divergence; and the parameter κ, set to either 1 or 0, is used to indicate the effect of the radial advection of $\overline{H}$ by perturbation flows. In ZZL, κ was set to null in order to obtain a second-order ordinary differential equation with constant coefficient, but $\kappa = 1$ is used herein.

As in ZZL, the basic state is in gradient wind balance; that is,

$$f\overline{V} + \overline{V}^2/r = gd\overline{H}/dr. \qquad (3)$$

Assuming the following harmonic form of wave solution,

$$\begin{aligned}\{u', v', h'\} &= \{u_n(r,t), v_n(r,t), h_n(r,t)\}\exp(in\lambda) \\ &= \{i\tilde{u}(r), \tilde{v}(r), \tilde{h}(r)\}\exp[i(n\lambda - \tilde{\omega}t)], \quad (4)\end{aligned}$$

where u_n, v_n, and h_n denote the perturbation amplitudes in terms of complex functions of radius and time, as in NMG, and $\tilde{u}$, $\tilde{v}$, and $\tilde{h}$ are the radial distribution of the perturbation amplitudes; n denotes the azimuthal WN; and $\tilde{\omega}$ is the Doppler-shifted wave frequency (s^{-1}), we obtain the azimuthal Fourier spatial version of the linearized perturbation equations [Eqs. (2a)–(2c)], as in SWVPAS; that is,

$$\begin{aligned}\frac{\partial u_n}{\partial t} &= -i\tilde{\omega}(i\tilde{u})\exp(in\lambda) \\ &= \left[-in\overline{\Omega}(i\tilde{u}) + \tilde{f}\tilde{v} - g\frac{d\tilde{h}}{dr}\right]\exp(in\lambda), \quad (5a)\end{aligned}$$

$$\frac{\partial v_n}{\partial t} = -i\tilde{\omega}\tilde{v}\exp(in\lambda) = \left[-in\overline{\Omega}\tilde{v} - \overline{\eta}(i\tilde{u}) - ig\frac{n\tilde{h}}{r}\right]\exp(in\lambda), \quad (5b)$$

$$\begin{aligned}\frac{\partial h_n}{\partial t} &= -i\tilde{\omega}\tilde{h}\exp(in\lambda) \\ &= \left\{-in\overline{\Omega}\tilde{h} - \frac{\overline{H}}{r}\frac{\partial}{\partial r}[r(i\tilde{u})] - \frac{d\overline{H}}{dr}(i\tilde{u}) - \frac{in\overline{H}}{r}\tilde{v}\right\}\exp(in\lambda). \quad (5c)\end{aligned}$$

To ensure the finite amplitudes of perturbation quantities, we require that $\tilde{h} = 0$ at $r = 0$ and as $r \to \infty$ for $n \geq 1$.

Because of the strong radial dependence of the dynamical variables in Eqs. (5a)–(5c), it is not possible to obtain analytical normal-mode solutions without making the following two assumptions as given in MK and ZZL: (i) the radial slow variation of all the dynamical variables and (ii) the nonzero local Doppler-shifted frequency. Thus, a numerical procedure has to be invoked. Here, the numerical solution technique of Flatau and Stevens' (1989) is used to solve Eqs. (5a)–(5c), with the same staggered grid configurations as those used by ML and NMG. That is, we first divide the domain $[0, r_b]$ equally into $2N$ pieces, giving the grid distance of $\delta r = r_b/2N$, and then define the horizontal winds at even grid points and the mass variables at odd grid points; namely,

$$\tilde{\omega}_{2k}\tilde{u}_{2k} = n(\overline{\Omega}\tilde{u})_{2k} + (\tilde{f}\tilde{v})_{2k} - g\frac{\tilde{h}_{2k+1} - \tilde{h}_{2k-1}}{\delta r}, \qquad (6a)$$
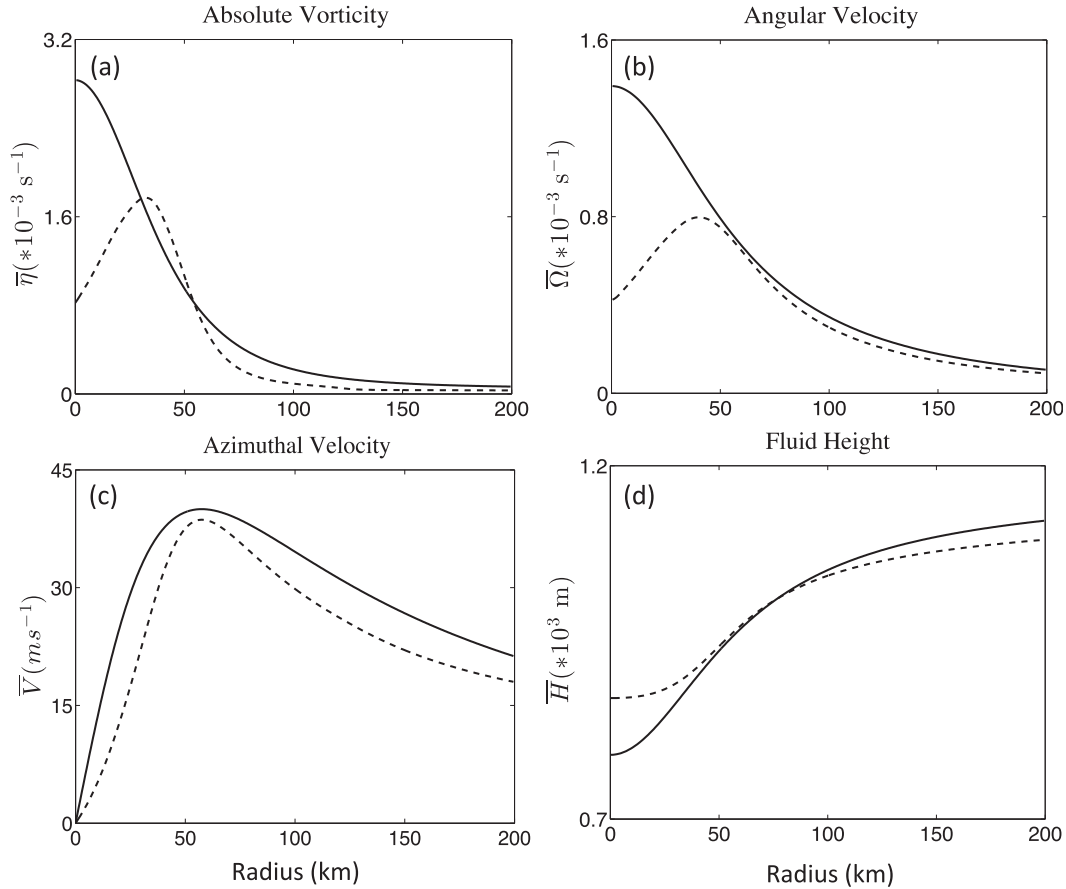
FIG. 1. Radial distribution of (a) absolute vorticity ($10^{-3}\,\mathrm{s}^{-1}$), (b) angular velocity ($10^{-3}\,\mathrm{s}^{-1}$), (c) azimuthal velocity ($\mathrm{m\,s}^{-1}$), and (d) fluid depth (m) associated with a monopolar vortex (solid) and a hollow (dashed) vortex as the basic state.

$$\tilde{\omega}_{2k}\tilde{v}_{2k} = n(\overline{\Omega}\tilde{v})_{2k} + (\overline{\eta}\tilde{u})_{2k} + \frac{ng}{r_{2k}}\frac{\tilde{h}_{2k+1}+\tilde{h}_{2k-1}}{2},$$

$$(6\mathrm{b})$$

$$\tilde{\omega}_{2k}\tilde{h}_{2k+1} = n(\overline{\Omega}\tilde{h})_{2k+1} + \frac{1}{r_{2k+1}}\frac{(r\overline{H}\tilde{u})_{2k+2}-(r\overline{H}\tilde{u})_{2k}}{\delta r}$$

$$+ \frac{n\overline{H}_{2k+1}}{r_{2k+1}}\frac{\tilde{v}_{2k+2}+\tilde{v}_{2k}}{2},$$

$$(6\mathrm{c})$$

where $k = 1, 2, \ldots, N$. The radial domain $[0, r_b]$ is truncated at an outer radius of $r_b = 2000\,\mathrm{km}$ where $\tilde{h}$ vanishes. As shown by ML, this domain size has little impact on the eigensolutions to be derived, provided that r_b is greater than the radius of Rossby deformation. Since we are only interested in the cases of $n > 0$, the boundary conditions are simply $\tilde{h}_1 = 0$ at $r = 0$ and $\tilde{h}_{2N+1} = 0$ at $r = r_b$. Then, the discretized system [Eqs. (6a)–(6c)] can be considered as a standard matrix eigenvalue problem; that is,

$$\tilde{\omega}\mathbf{X} = \mathbf{A}\mathbf{X}, \qquad (7)$$

where $\tilde{\omega}$ can also be understood as eigenfrequency, $\mathbf{X} = (\tilde{u}_2, \tilde{v}_2, \tilde{h}_2, \ldots, \tilde{u}_{2N}, \tilde{v}_{2N})^{\mathrm{T}}$ is the eigenfunction of the discretized system, and $\mathbf{A}$ is a $(3N - 1) \times (3N - 1)$ matrix representing discretization of the differential operator of Eqs. (6a)–(6c) with the boundary conditions included. The matrix eigenvalue problem is numerically solved using SWVPAS, whose functions have been improved herein to include all resolvable eigenvalues.

It is evident from Eq. (7) that each $\tilde{\omega}$ of $\mathbf{A}$ represents one frequency of the discretized, linearized shallow-water equations, and that a full spectrum of wave frequencies can be obtained by solving this eigenequation. By varying the size of N, we can minimize the distortion of frequency spectrum caused by numerical discretization. We find that the use of $N = 2000$ with $\delta r = 1\,\mathrm{km}$ is satisfactory for this purpose.

Next, we need to consider the impact of a basic-state or mean vortex on wave frequencies and structures. Two types of vortex profiles—that is, monopolar and hollow

in terms of $\overline{\eta}$ (Fig. 1a)—have been previously used for wave-motion studies. In a monopolar vortex, both $\overline{\eta}$ and $\overline{\Omega}$ are peaked at the center and they decrease outward with radius, thus exhibiting large negative radial gradients in $\overline{\Omega}$ (Fig. 1b) within the radius of maximum wind (RMW or r_m). Figure 1c shows the radial distribution of azimuthal flow, $\overline{V} = [2R/(1 + R^2)]\overline{V}_{\max}$, as used by MK, where $\overline{V}_{\max} = 40\,\mathrm{m\,s^{-1}}$ is the maximum azimuthal flow at the RMW and $R = r/r_m$ is the nondimensional radius. Figure 1d shows the corresponding height field that is in gradient balance with the azimuthal flow. This type of vortex profile has been shown by MK and ML to favor the generation and propagation of VRWs, and it will be shown herein to also allow for the generation and propagation of mixed VRIGWs.

In contrast, a hollow vortex is characterized by a minimum in $\overline{\eta}$ at the vortex center and a maximum at the radius of maximum vorticity (RMζ) that is located slightly inside the RMW. Hollow vortex profiles have been used to examine the local frequency relation of IGWs, VRWs, and VRIGWs by ZZL and the dynamics of barotropic or algebraic instability in TCs by Schubert et al. (1999), NMG, Nolan and Montgomery (2002), and Zhong et al. (2010). Figure 1 shows an example of a hollow vortex, with $r_m = 57.5\,\mathrm{km}$, that is based on the simulation of Hurricane Andrew (1992) by Liu et al. (1997). Note that its peak $\overline{\eta}$, shown in Fig. 1a, has been significantly reduced from that used by ZZL in order to obtain $\overline{V}_{\max}$ at the RMW that is similar in magnitude to that of MK's monopolar vortex (Fig. 1c) for the subsequent comparison of wave motions on the two different basic states. This alteration in the basic-state intensity is necessary because the generation and propagation of VRWs and VRIGWs differ from the other typical linear oscillators whose "natural frequency depends only on the physical characteristics of the oscillator, not on the motion itself" (Holton 2004). Specifically, although the propagation of VRWs is described as an analogy to that of Rossby waves, their restoring forces are essentially determined by the mean flow. This is because the latter owes its existence to the meridional gradient of the Coriolis force, which has little to do with the large-scale mean flow. By comparison, VRWs are determined by the radial gradients of $\overline{\eta}$ in TCs, implying that the radial distribution of the mean rotational flow governs the natural frequency of VRWs, and similarly for VRIGWs.

Note the two distinct $\overline{\eta}$ radial structures that correspond to the two seemingly similar $\overline{V}$ profiles, especially within the RMW (cf. Figs. 1a and 1c). A close scrutiny of Fig. 1c reveals that the $\overline{V}$ slope for the monopolar vortex begins with a finite value at $r = 0$ and then decreases with radius, whereas for the hollow vortex, it manifests an outward increasing tendency at $r = 0$ and attains a peak
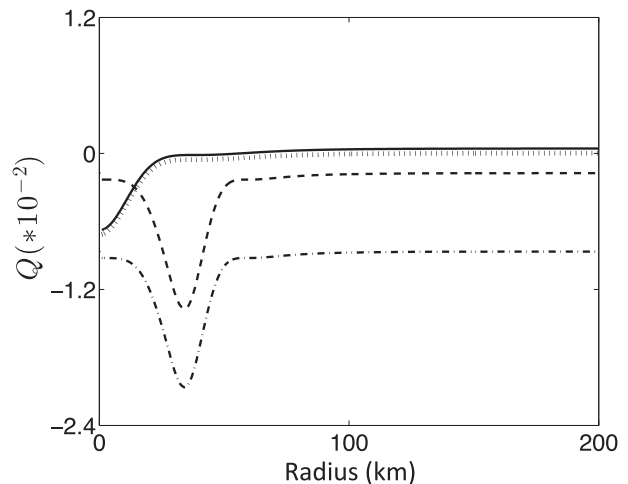

FIG. 2. Radial distribution of discriminant Q (10^{-2}) for the cubic frequency equation [Eq. (1b)], given the values of $m = 0.8$ and WN $n = 1, 2$, associated with the monopolar and hollow vortices shown in Fig. 1. Solid (WN 1) and dotted (WN 2) lines are for the monopolar vortex, and dashed (WN 1) and dotted–dashed (WN 2) lines are for the hollow vortex.

value before reaching the RMW. Although both $\overline{V}$ profiles may be common in TCs, they have quite different dynamical implications in terms of wave propagation and stability, as will be shown herein.

Figure 1d compares the height fields between the monopolar and hollow vortices. Because of the larger amplitude of $\overline{V}$ and thus $d\overline{H}/dr$ outward from the RMW, the mean height field in the hollow vortex is lower than that in the monopolar vortex (cf. Figs. 1c and 1d), except in the core region where an opposite occurs.

At this point, one may wonder if the monopolar vortex would also allow the development of VRIGWs. For this purpose, we have repeated all the calculations as those in ZZL, including the radial distribution of the Bessel parameter and several nondimensional parameters given in Eq. (1) and found little qualitative differences in these parameters between the monopolar and hollow vortices (not shown), except that the former has no singularity near R_0 (see Fig. 2b in ZZL for an example at the RMζ associated with a hollow vortex). Figure 2 shows that the existence of such a singularity does affect the radial distribution and magnitude of Q between the two types of vortices but affects little the theoretical implication of mixed-wave motions. That is, the condition of $Q \leq 0$ takes place in the core region of the monopolar vortex, albeit with much smaller magnitudes, as compared to the eyewall region near the RMW of the hollow vortex. Note that the value of Q in Fig. 2, calculated with $m = 0.8$, is one order of magnitude smaller than that calculated with $m = 1.5$ in Fig. 7 of ZZL. This difference could be attributed to the use of
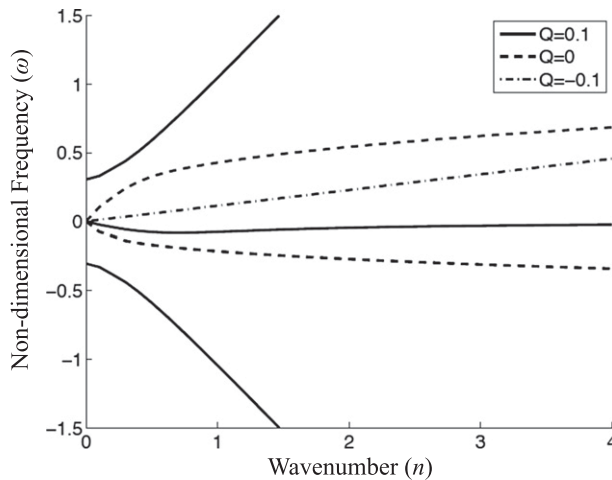
FIG. 3. Nondimensionized intrinsic frequency as a function of azimuthal WN, based on Eq. (1a), in association with the monopolar vortex given in Fig. 1 for $Q = 0.1$ (solid), $Q = 0$ (dashed), and $Q = -0.1$ (dotted–dashed).

large $\overline{\eta}$ for the hollow vortex. Nevertheless, it follows that monopolar vortices could also support the development of mixed VRIGWs and mixed-wave instability, although they tend to occur more readily in hollow vortices in the vicinity of large $\overline{\eta}$. The mixed-wave instability will be a separate subject for a future study. Thus, we may state that VRIGWs can develop in both monopolar and hollow vortices, provided that the condition of $Q \leq 0$ is met, depending upon the combination of their basic-state parameters and m [see Eq. (1b)].

To see further the generation of VRIGWs in relation to the other two classes of pure waves in the monopolar vortex, Fig. 3 shows a frequency–WN diagram for three different values of Q, based on Eq. (1), in which ω denotes the nondimensional intrinsic wave frequency; see Fig. 6 in ZZL for a similar diagram associated with a hollow vortex. When $Q > 0$, there are a pair of high-frequency IGWs propagating in opposite directions and a low-frequency VRW propagating against the mean flow. The two classes of waves have fundamentally different frequency distributions with WN n. That is, the frequencies of IGWs increase rapidly from the value of f at WN 0, whereas the VRW frequency increases slowly from the origin and reaches a peak at WN 1 and then decreases slowly with WN n. In the case of $Q = 0$, we see two allowable waves with frequencies increasing slowly at higher WNs but faster at lower WNs, which are similar in physical characteristics to those of VRWs and IGWs, respectively; they are so-called mixed VRIGWs. The mixed waves occur in the vicinity of the peak $\overline{\eta}$, regardless of a monopolar or hollow vortex, making rotation as the primary factor for lower-WN waves. This differs from the equatorial Rossby–gravity waves, in

which gravitation acts as the main restoring force for lower-WN waves, especially at the equator where the planetary vorticity vanishes. When $Q < 0$, there are a mixed VRIGW propagating in the same direction as the mean flow (dashed–dotted lines in Fig. 3) and a pair of growing (decaying) mixed waves (not shown). All of these properties are similar to those of a hollow vortex shown in Fig. 6 of ZZL.

3. Spectrum and eigenmode structures of free waves

In this section, we examine the wave spectrum and eigenmode structures in the discretized system [Eqs. (6)] with the monopolar and hollow vortices as the basic state, respectively.

a. Wave spectral analysis

Wave spectrum represents the aggregation of eigenvalues for **A** in Eq. (7), and each spectral point can be viewed as one eigenvalue or one wave frequency in the wave dynamics of TCs. Similarly, an eigenfunction represents the spatial distribution of a wave's perturbation fields. By analyzing the eigenvalue and eigenfunction of Eq. (6) with SWVPAS, we may gain insight into the spectral distribution of various classes of free waves propagating as described by Eq. (2).

By definition (Zeng et al. 1990; Eidelman et al. 2004), when the resolvent $(\mathbf{AX} - \tilde{\omega}\mathbf{I})^{-1}$, where $\mathbf{I}$ is an identity matrix, is bounded, $\tilde{\omega}$ has a set of eigenvalues for **A** in Eq. (7) that can be characterized by point spectrum. When the resolvent is infinite or **A** has a singularity with the spatial dependence of basic-state flows, $\tilde{\omega}$ is characterized by continuous or dense spectrum. It is evident that when the basic state is at rest, all free waves described by Eq. (6) are in the point spectrum of **A** with sparse distribution, and VRWs should be absent in a resting basic state. Figure 4a shows the wave spectral distribution for such a resting flow, following ML. Obviously, the sparsely distributed spectral points on both sides of the $\tilde{\omega} = 0$ solution should be associated with IGWs, with the two spectrum points at $\tilde{\omega} = \pm 5 \times 10^{-5}\,\mathrm{s}^{-1}$ corresponding to a pair of pure inertial waves. In addition, the frequencies of IGWs increase with WN n, which is consistent with the theory of IGWs (Pedlosky 2003) and the eigenmode analysis of ML.

However, the wave spectral structures become complicated in the presence of nonvanishing mean flows. If $\overline{\Omega}_{\max}$ and $\overline{\Omega}_{\min}$ are defined as the respective upper and lower limit of the basic-state angular velocity, we can see different wave spectral characteristics over the following two frequency ranges: (i) $\tilde{\omega} > n\overline{\Omega}_{\max}$ or $\tilde{\omega} < n\overline{\Omega}_{\min}$, and (ii) $n\overline{\Omega}_{\min} \leq \tilde{\omega} \leq n\overline{\Omega}_{\max}$. In the first scenario, we must
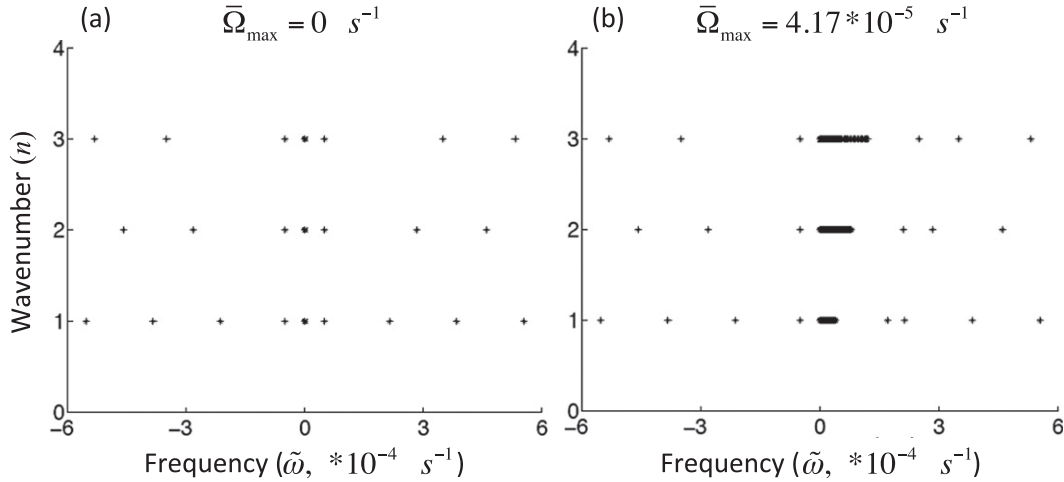
FIG. 4. Eigenfrequency scatterplots as a function of WN ($n = 1$–3) associated with (a) a resting basic state (i.e., $\overline{\Omega}_{max} = 0\,\mathrm{s}^{-1}$) and (b) a weak monopolar vortex (i.e., $\overline{\Omega}_{max} = 4.17 \times 10^{-5}\,\mathrm{s}^{-1}$).

have $\tilde{\omega} - n\overline{\Omega} \neq 0$, implying that there is no singularity after plugging the wave frequencies into Eqs. (6), and the resulting eigenvalues must be in the point spectrum of **A**. A comparison of the wave spectrum between Figs. 4a and 4b indicates that the frequency ranges of $\tilde{\omega} > n\overline{\Omega}_{max}$ or $\tilde{\omega} < n\overline{\Omega}_{min}$ must be associated with IGWs. In contrast, when $n\overline{\Omega}_{min} \leq \tilde{\omega} \leq n\overline{\Omega}_{max}$, there must exist a point $r = r_c$, at which $\tilde{\omega} - n\overline{\Omega}\,(r_c) = 0$, implying that a singularity occurs at r_c—the so-called critical radius (ML). In this case, only an integration of its eigenfunction over the spectrum range can constitute the particular solution of Eqs. (6) (Zeng et al. 1990). Thus, the pertinent eigenvalues are distributed in the continuous spectrum of **A**, and associated with VRWs (Fig. 4b).

The above discussion is consistent with theories of VRWs and IGWs. For the former, MK derived the following Doppler-shifted frequency $\tilde{\omega}_R$ relation near the radius of $r = r_0$ from the nondivergent barotropic vorticity equation,

$$\tilde{\omega}_R = n\overline{\Omega}_0 + \overline{\omega}_R = n\overline{\Omega}_0 + \frac{nd\overline{\eta}_0/dr}{r_0(l^2 + n^2/r_0^2)}, \qquad (8)$$

where $\overline{\omega}_R$ is the dimensional intrinsic frequency of VRWs; $\overline{\Omega}_0$, $d\overline{\eta}_0/dr$, and the other variables with the subscript 0 will be treated as constant in the vicinity of $r = r_0$ as assumed in MK and ZZL; and l is the radial WN. Clearly, VRWs owe their existence to the radial gradient in $\overline{\eta}$. According to Wang (2001), both WN 1 and WN 2 waves propagate against the mean flows of TCs at the phase speed of about $34\,\mathrm{m\,s}^{-1}$, which corresponds to a frequency range of 10^{-3}–$10^{-4}\,\mathrm{s}^{-1}$. It is apparent from Figs. 1 and 4b that VRWs occur mostly within $r = 100$ km where the radial gradient in $\overline{\eta}$ is much greater than

that in the outer region, and that the wave frequency decreases with WN. Since VRWs propagate against the mean flow, their Doppler-shifted frequencies should have the range of $\tilde{\omega}_R \in [0, n\overline{\Omega}_{max}]$ in a monopolar vortex. This suggests that the maximum mean angular velocity, occurring near the TC center, determines the upper limit of $\tilde{\omega}_R$ with a critical radius r_c. In addition, Schecter and Montgomery (2004) indicated that VRWs tend to be damped at $r = r_c$, so little perturbation structures of VRWs could be seen beyond $r = r_c$. We can also see from the above scale analysis that $\tilde{\omega}_R$ at lower WN should have a magnitude of 10^{-4}–$10^{-5}\,\mathrm{s}^{-1}$, and $\tilde{\omega}_R$ would approach $n\overline{\Omega}_0$ at higher WN. In contrast, for a hollow vortex, the sign change of $d\overline{\eta}_0/dr$ may cause $\tilde{\omega}_R$ to exceed the magnitude of $n\overline{\Omega}_{max}$, and wave breaking may occur in the presence of barotropic instability. It follows that VRWs can only take place in the continuous spectrum with $\tilde{\omega}_R \in [0, n\overline{\Omega}_{max}]$ for monopolar vortices (Fig. 4b), but the wave frequency may exceed $n\overline{\Omega}_{max}$ for hollow vortices.

Next, let us examine the spectral characteristics of IGWs in the presence of strong rotational flows. ZZL have given the following frequency relation for IGWs,

$$\tilde{\omega}_G = n\overline{\Omega}_0 + \overline{\omega}_G = n\overline{\Omega}_0 \pm \sqrt{c_0^2\overline{m}_0^2 - \eta_0^2\overline{\Omega}_0^2}, \qquad (9)$$

where $\overline{m} = m/R_m$ is the dimensional form of $m(n)$, and c_0^2 is the phase velocity of surface gravity waves and is considered as a constant.

Evidently, the IGW frequencies are closely associated with vortex intensity. It can be shown that when the rotational flow is weak, $\overline{\Omega}_{max}$ will be smaller than the threshold value of $\overline{\Omega}_l = c_0\overline{m}\sqrt{n^2 + 3}$ (see appendix). Thus, we may have $\tilde{\omega}_G > n\overline{\Omega}_{max}$, which is distinct from
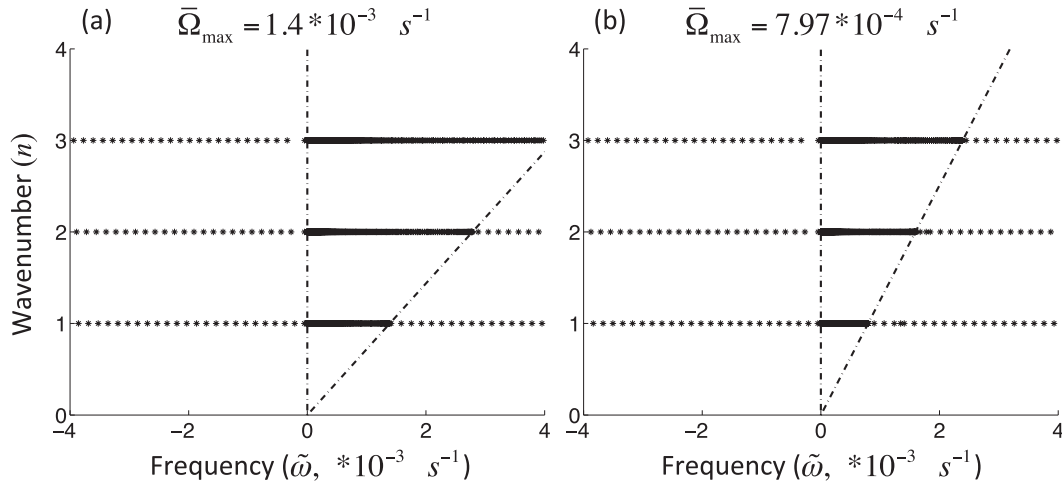
FIG. 5. As in Fig. 4b, but for (a) the monopolar vortex with $\overline{\Omega}_{max} = 1.4 \times 10^{-3}\,s^{-1}$, and (b) the hollow vortex with $\overline{\Omega}_{max} = 7.97 \times 10^{-4}\,s^{-1}$, as given in Fig. 1.

the continuous spectrum of low-frequency VRWs. This analysis confirms the earlier result that IGWs are in the discrete spectrum of **A**. With the typical values of $c_0 \sim 10^2\,\mathrm{m\,s^{-1}}$, $m \sim 10^{-1}$, $\overline{m} = m/R_m \sim 10^{-6}$, and $n \sim 10^0$, the threshold value of $\overline{\Omega}_l$ is about 10^{-4}–$10^{-5}\,s^{-1}$, and it decreases with increasing WN n. Thus, the IGW frequencies tend to move toward the lower-frequency range for strong TCs and enter the range of continuous spectrum when the basic-state rotation exceeds $\overline{\Omega}_l$. As a result, these waves may increasingly be influenced by rotation, leading to the development of mixed characteristics of IGWs and VRWs.

Based on the above analysis, we may see the following three scenarios. First, for a monopolar vortex, when its intensity satisfies $\overline{\Omega}_{max} < \overline{\Omega}_l = c_0\overline{m}\sqrt{n^2 + 3}$, high-frequency IGWs and low-frequency VRWs can be clearly separated with the presence of mixed VRIGWs. IGWs will be distributed discretely in the spectral region of $\tilde{\omega}_G > n\overline{\Omega}_{max}$ and $\tilde{\omega}_G < 0$, whereas VRWs will appear in the continuous spectrum range $[0, n\overline{\Omega}_{max}]$. Second, when the vortex intensity exceeds a threshold value, the frequency of IGWs would "red shift" into the continuous spectral region, especially at higher WNs. Then, mixed VRIGWs and mixed-wave instability may occur in the case of $Q \leq 0$ (ZZL). This is the main reason for the generation of mixed VRIGWs in both monopolar and hollow vortices. Third, the sign change of $d\overline{\eta}_0/dr$ across the RMζ in a hollow vortex could generate two oppositely propagating VRWs on each side, making $\tilde{\omega}_R$ exceed $n\overline{\Omega}_{max}$. Thus, the "violet shift" of VRWs, as a result of the increased influence of gravitation, is another reason for the development of mixed VRIGWs. Figure 4b does show three wave spectral regions on a weak monopolar vortex ($\overline{\Omega}_{max} = 4.17 \times 10^{-5}\,s^{-1}$) for

WN $n = 1$–3: the continuous spectrum between 0 and $n\overline{\Omega}_{max}$, and two discrete spectra outside, which correspond to a low-frequency VRW and two high-frequency IGWs, respectively.

However, Fig. 5a shows that the wave spectral structures change substantially when the vortex intensity exceeds a threshold. Although the wave spectrum still exhibits continuous and discrete distributions inside and outside the range $[0, n\overline{\Omega}_{max}]$, respectively, much less distinction occurs between the two. In particular, higher-frequency waves tend to red shift into the continuous spectrum for both monopolar and hollow vortices. It should be mentioned that ML have shown some similar results for an intense monopolar vortex (see their Fig. 4), but they focused on the balanced and unbalanced aspects of VRWs and IGWs, respectively. For an intense hollow vortex, lower-frequency waves also show a violet shift into the discrete spectral region (Fig. 5b). In this case, IGWs have frequencies similar to those of VRWs such that one cannot clearly distinguish the "fast" propagating IGWs from "slow" propagating VRWs. Thus, we may consider these waves as being influenced by both rotation and gravitation, leading to the formation of mixed VRIGWs. Because their frequencies decrease with increasing WN n, shorter VRWs tend to have more mixed VRIGWs properties.

b. Eigenmode analysis

Since both observational and modeling studies show the slower-than-mean-flow propagation of disturbances in the eyewall (i.e., with positive Doppler-shifted frequencies), we may simply examine the eigenstructures of the three classes of waves as being characterized by their amplitudes: high, intermediate, and low frequencies,
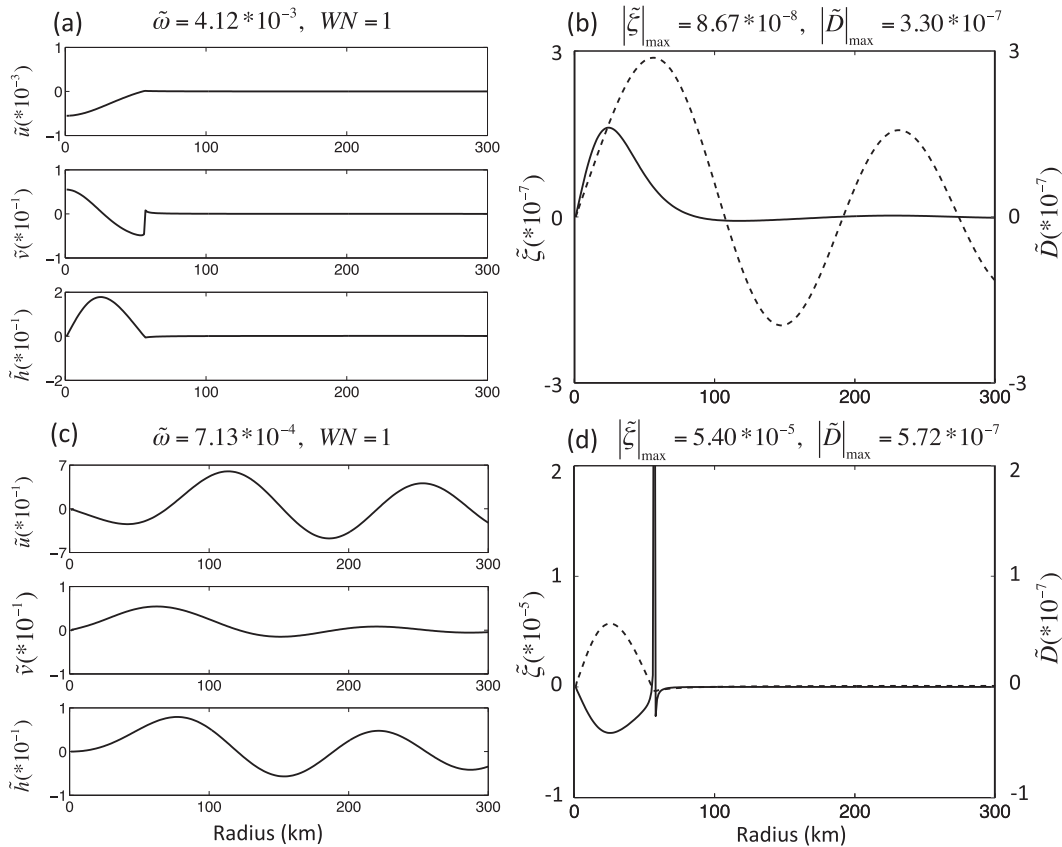
FIG. 6. Radial distribution of (a),(c) the perturbation radial and azimuthal wind speeds (m s^{-1}) and the perturbation height (m) and (b),(d) relative vorticity (s^{-1}; solid) and divergence (s^{-1}; dashed) for WN 1 waves on the monopolar vortex given in Fig. 1, with (a),(b) a high frequency ($\tilde{\omega} = 4.12 \times 10^{-3}$ s^{-1}) and (c),(d) a low frequency ($\tilde{\omega} = 7.13 \times 10^{-4}$ s^{-1}).

respectively. High-frequency waves include discrete spectral points that are greater than $n\overline{\Omega}_{max}$, whereas both the intermediate- and low-frequency waves appear in the advective frequency range $[0, n\overline{\Omega}_{max}]$. However, at WN 1, almost all the eigenstructures can be grouped into two classes as separated by the advective frequency $n\overline{\Omega}_{max}$. So we choose $\tilde{\omega} = 4.12 \times 10^{-3}$ and 7.13×10^{-4} s^{-1} as two representative waves and plot their radial structures in Figs. 6a and 6b and in Figs. 6c and 6d, respectively.

It is apparent that the high-frequency WN-1 wave exhibits radial wavelike structures for the perturbation variables $\tilde{u}$, $\tilde{h}$, and $\tilde{D}$ with slow decreases in amplitude (Figs. 6a,b). But the wavelike structures for the perturbation variables $\tilde{v}$ and $\tilde{\zeta}$ are only notable in the inner-core region with their amplitudes decrease sharply outward (e.g., for $\tilde{\zeta}$ from 10^{-7} to 10^{-8} s^{-1} inside $r = 100$ km and then to 10^{-9} s^{-1} outside $r = 100$ km). Although divergence is slightly smaller than $\tilde{\zeta}$ within $r = 30$ km, it is one to two orders of magnitude greater than $\tilde{\zeta}$ outside because of its slow outward decreases. Thus, the high-frequency wave on a monopolar vortex exhibits the

typical characteristics of IGWs. In particular, divergence is well correlated with $\tilde{h}$ field, with a convergent (divergent) flow corresponding to a lower (higher) free surface. In addition, $\tilde{h}$ is in phase with $\tilde{\zeta}$ in the core region [i.e., with positive (negative) $\tilde{h}$ corresponding to cyclonic (anticyclonic) flows], implying that the high-frequency wave is unbalanced. Other high-frequency WN-1 waves behave similarly (not shown), except for possessing shorter radial wavelengths than those shown in Figs. 6a and 6b.

In contrast, the low-frequency wave has little radial wavelike structures (Figs. 6c,d), which confirms the earlier analysis of the dispersion relation of VRWs. As mentioned before, each VRW mode has a critical radius r_c, at which the Doppler-shifted frequency vanishes. In fact, r_c is determined by wave frequency, and it is smaller for higher frequency. At r_c, $\tilde{v}$ is discontinuous, and a cusp appears for both $\tilde{u}$ and $\tilde{h}$. More importantly, all perturbation variables show wavy structures only within r_c, suggesting that VRWs can develop only in the monopolar core region. Unlike IGWs, $\tilde{\zeta}$ has a sharp change in

sign and magnitude near r_c and is about two orders of magnitude greater than that of divergence. In addition, $\tilde{h}$ and $\tilde{\zeta}$ are opposite in phase, with positive (negative) $\tilde{h}$ corresponding to negative (positive) $\tilde{\zeta}$ except at r_c, indicating that the low-frequency wave is balanced and rotationally dominated. All of these are the typical characteristics of VRWs.

A critical radius also occurs for the intermediate-frequency WN-1 wave, whose Doppler-shifted frequency is close to $n\overline{\Omega}_{max}$, but on average about twice greater than that of the low-frequency wave. Of importance is that the intermediate-frequency wave behaves in the same way as a VRW, with $\tilde{\zeta}$ being at least one order of magnitude greater than divergence within r_c. Outside it, however, the wavelike structures are similar to those of IGWs, with much smaller $\tilde{\zeta}$ than divergence. Thus, the intermediate-frequency waves are of the mixed-VRIGW class in the continuous spectrum that is caused by the red shift of IGWs. Nevertheless, this class of mixed wave differs from the theoretical mixed VRIGWs in ZZL, and it appears only at a small number of spectral points. So, we do not consider this class of WN-1 mixed waves herein as they are not as common as VRWs and IGWs in monopolar vortices.

However, as the azimuthal WN increases, the decreased frequency of VRWs and the extended frequency range of IGWs make some of their radial wave structures differ from those of WN-1 waves. Figure 7 shows WN-2 wave structures associated with a high-frequency wave at $\tilde{\omega} = 5.26 \times 10^{-3}\,\mathrm{s}^{-1}$ (Figs. 7a,b), an intermediate-frequency wave at $\tilde{\omega} = 1.54 \times 10^{-3}\,\mathrm{s}^{-1}$ (Figs. 7c,d), and a low-frequency wave at $\tilde{\omega} = 3.25 \times 10^{-4}\,\mathrm{s}^{-1}$ (Figs. 7e,f). Although the radial structures of the high-frequency WN-2 wave are similar to its corresponding WN-1 structures (cf. Figs. 7a,b and 6a,b), its $\tilde{\zeta}$ becomes much smaller than divergence outward from $r = 30\,\mathrm{km}$, indicating an important gravitational impact at higher WNs.

Figures 7c and 7d show an example of intermediate-frequency wave with $r_c = 50\,\mathrm{km}$. Its perturbation structures within and near r_c are similar to those shown in Figs. 6c and 6d except for the half- versus one-quarter wavelength oscillation of $\tilde{u}$ and $\tilde{v}$ owing to the null value of $\tilde{u}$ and $\tilde{v}$ at $r = 0$. The presence of very high amplitude of $\tilde{\zeta}$ and the antiphased relationship between $\tilde{\zeta}$ and $\tilde{h}$ suggests that this intermediate-frequency wave has the typical characteristics of VRWs. The frequency shift of VRWs—for example, from the low frequency at WN 1 (Figs. 6c,d) to the intermediate frequency at WN 2 (Figs. 7c,d)—can be easily understood from Eq. (8), indicating that the intrinsic frequency of pure VRW sharply decreases as WN increases. As a result, its

Doppler-shifted frequency approaches to the advective frequency at higher WNs with decreasing r_c.

The low-frequency WN-2 wave also has a critical radius, at which $\tilde{v}$ is again discontinuous whereas $\tilde{h}$ and $\tilde{u}$ are minimized and maximized, respectively (Figs. 7e,f). However, this r_c appears in the outer region, near $r = 180\,\mathrm{km}$, rather than in the inner-core region. Just like the VRW in Fig. 7c, the discontinuity of $\tilde{v}$ and a jump in $\tilde{\zeta}$ also occur near r_c. Despite the outward shift of r_c, the inner-core region is dominated by convergence with its magnitude decreasing rapidly toward r_c. Although the magnitude of $\tilde{\zeta}$ is small and similar to that of $\tilde{D}$ in the inner-core region, it is large and much greater than that of $\tilde{D}$ near r_c. Moreover, $\tilde{\zeta}$ keeps positive while $\tilde{h}$ fluctuates within r_c, indicating that the cyclonic flows corresponds to a low pressure region, like VRWs, and to a high pressure region, like IGWs, respectively, inside and outside $r = 60\,\mathrm{km}$. Thus, this mode should be regarded as a mixed VRIGW in the core region. Similar features can also be found for higher-WN waves (not shown). It follows that at higher WN, low-frequency waves tend to exhibit more mixed-wave characteristics. ML also examined the low-frequency waves at WN 2 and higher, and found this "unexpected" mixed-wave structure in their Rossby shear modes. However, the theoretical framework ML used to understand VRWs, which is based on nondivergent absolute vorticity equation, cannot describe the fundamental properties of mixed VRIGWs. So ML could only speculate the existence of some commonalities with equatorial mixed Rossby–gravity waves found by Matsuno (1966).

Figure 8 shows the WN-2 eigenmodes of intermediate- and low-frequency waves on the hollow vortex for the purpose of comparing them to those on the monopolar vortex given in Figs. 7c–f. Only their propagation solutions are selected because of the presence of mixed-wave instability near the RMζ where $d\overline{\eta}_0/dr$ changes sign leading to $Q < 0$ (see Fig. 5 in ZZL). In this regard, use of monopolar vortices may be more suitable for theoretical studies of wave motions. We see that the general wave structures, the larger magnitude of $\tilde{\zeta}$ near the RMW, and the phase configuration of $\tilde{h}$ and $\tilde{\zeta}$ associated with the hollow vortex are similar to those given in Figs. 7c–f, except for more local singularities near the RMW and r_c. This indicates that these intermediate- (Figs. 8a,b) and low- (Figs. 8c,d) frequency waves correspond to VRWs and mixed VRIGWs, respectively.

This mixed-wave mode could play an important role in geostrophic adjustment as discussed by ML, but in different ways over different regions of a hollow vortex. Here, let us consider a rapidly rotating vortex by defining $\hat{f}^2 = \tilde{f}\overline{\eta}$ as the rotation intensity. Following ML, we define the ratio of wave intrinsic frequency to
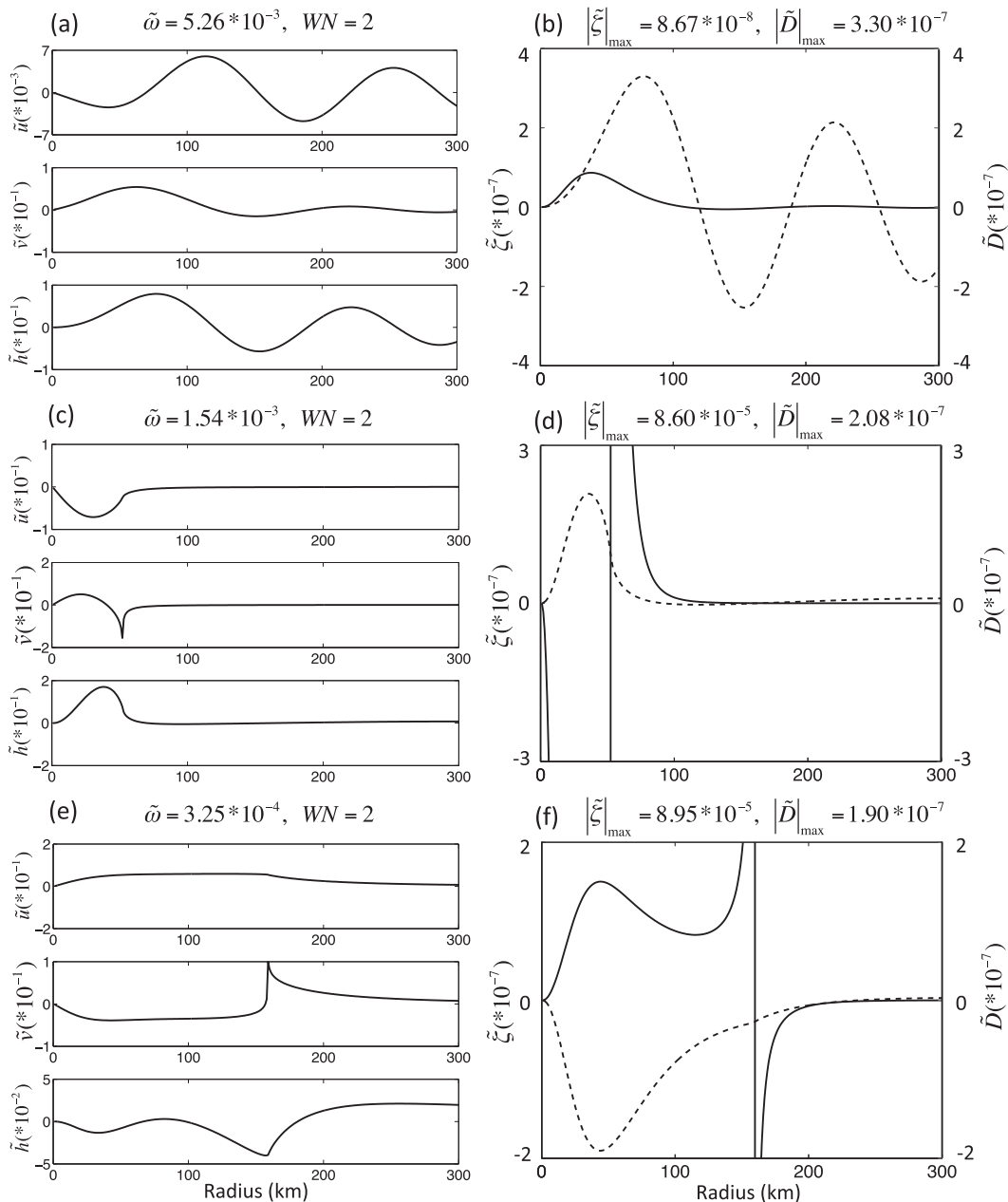
FIG. 7. As in Fig. 6, but for WN-2 waves with (a),(b) a high frequency (i.e., $\tilde{\omega} = 5.26 \times 10^{-3}\,\text{s}^{-1}$); (c),(d) an intermediate frequency (i.e., $\tilde{\omega} = 1.54 \times 10^{-3}\,\text{s}^{-1}$); and (e),(f) a low frequency (i.e., $\tilde{\omega} = 3.25 \times 10^{-4}\,\text{s}^{-1}$).

rotation intensity as the nondimensional adjustment criterion, i.e., $S^2 = \overline{\omega}^2/\hat{f}^2$. When $S^2 < 1$, the wave motion is more balanced, like VRWs, with positive (negative) $\tilde{h}$ coinciding with negative (positive) $\tilde{\zeta}$. However, when $S^2 > 1$, the mass and wind fields are unbalanced, and IGWs should exert more influences on the adjustment. To help visualize the above points, Fig. 9 shows the radial distribution of S^2 associated with the low-frequency modes for the monopolar (as in Figs. 7e,f) and hollow (as

in Figs. 8c,d) vortices. Both contours exhibit wavelike radial distributions of S^2. Of particular relevance is that S^2 is less than unity in the core region (i.e., 0–50 km) and near r_c (i.e., 100–200 km), whereas it is greater than unity elsewhere. Clearly, these features reflect the balanced and unbalanced characteristics of the mixed-wave mode, corresponding to the respective roles of VRWs and IGWs at different radii of the vortices. Thus, this mode should not be classified as a VRW mode as ML.
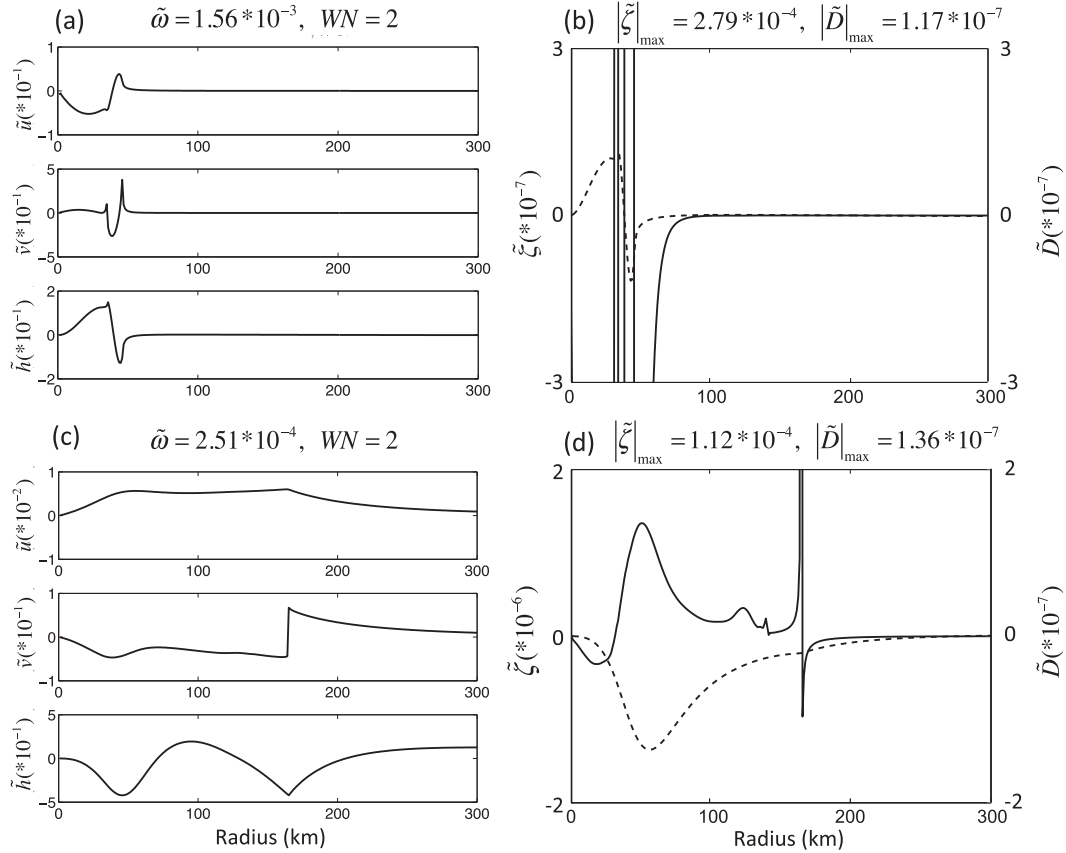
FIG. 8. As in Fig. 6, but for (a),(b) a WN-2 VRW with $\tilde{\omega} = 1.56 \times 10^{-3}\,\mathrm{s}^{-1}$ and (c),(d) a WN-2 mixed VRIGW with $\tilde{\omega} = 2.51 \times 10^{-4}\,\mathrm{s}^{-1}$ on the hollow vortex given in Fig. 1.

4. Propagation of WN-2 waves on the monopolar and hollow vortices

After showing the single wave structures of eigenmodes associated with the monopolar and hollow vortices, it is of interest to compare the propagation characteristics of the three classes of waves on the two different types of vortices. In addition, it is desirable to compare the wave solutions obtained herein to the analytical solutions derived in ZZL. Given initial perturbations, two additional approaches can be used, besides the analytical solutions, to examine the wave propagation characteristics for a set of discretized eigenmodes at an azimuthal WN: One is to linearly superimpose them via the wave solutions equation [Eq. (4)], and the other is to numerically integrate them using SWVPAS. Specifically, in the former case, with the staggered grid arrangements used herein, we may rewrite Eq. (4) as MK with the form of

$$u'(r_k, t) = \sum_{a=1}^{3} \sum_{b=1}^{B_a} C_b \tilde{u}_{k,b} \exp(-i\tilde{\omega}_b t), \quad (10a)$$

$$v'(r_k, t) = \sum_{a=1}^{3} \sum_{b=1}^{B_a} C_b \tilde{v}_{k,b} \exp(-i\tilde{\omega}_b t) \quad (10b)$$

at N wind grid points ($k = 1, 3, 5, \ldots, 2N - 1$), and

$$h'(r_k, t) = \sum_{a=1}^{3} \sum_{b=1}^{B_a} C_b \tilde{h}_{k,b} \exp(-i\tilde{\omega}_b t) \quad (10c)$$

at the $N - 1$ height grid points ($k = 2, 4, 6, \ldots, 2N - 2$). Here, a is the wave index, whose value of 1–3 represents IGWs, VRWs, and mixed VRIGWs, respectively; b is the eigenfrequency index ranging from 1 to B_1, from 1 to B_2, and from 1 to B_3; B_1, B_2, and B_3 are the total eigenmodes of IGWs, VRWs, and mixed VRIGWs, respectively, as classified by eigenfrequencies in Fig. 5 and wave characteristics in Fig. 7 or Figs. 8c and 8d, and they satisfy $B_1 + B_2 + B_3 = 3N - 1$; ($\tilde{u}_{k,b}, \tilde{v}_{k,b}, \tilde{h}_{k,b}$) represent the radial component of an eigenvector at WN-2; k is the radial index; and the coefficient C_b should be typically inverted from Eq. (10) for the given initial perturbations $u'(r_k, 0), v'(r_k, 0)$, and $h'(r_k, 0)$. Clearly, the propagation
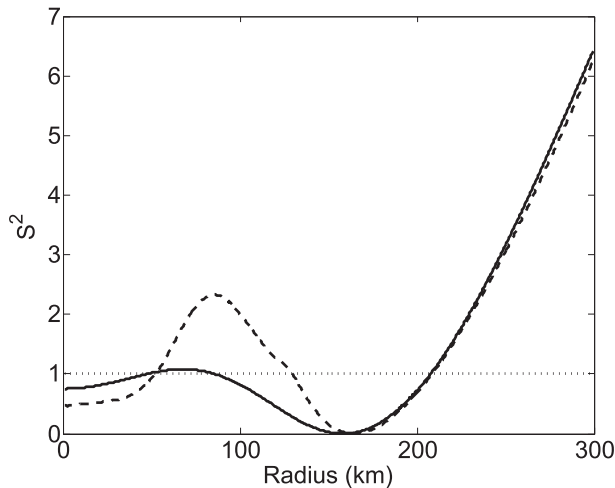
FIG. 9. Radial distribution of the nondimensional adjustment parameter for WN-2 low-frequency waves on the monopolar vortex ($\tilde{\omega} = 3.25 \times 10^{-4}\,\mathrm{s}^{-1}$, solid) and hollow vortex ($\tilde{\omega} = 2.51 \times 10^{-4}\,\mathrm{s}^{-1}$, dashed) (see Figs. 1, 7e,f, and 8c,d).

of a pure class of waves can be examined by superimposing the same class of eigenvectors and eigenvalues obtained through SWVPAS and then composited by Eq. (10), like the analytical solutions of ZZL.

In contrast, numerical integrations of the SWVPAS model from the initial composite perturbations cannot guarantee the propagation of a pure class of waves, even started from a pure one, because the model contains the dynamical mechanisms for the generation of all the three classes of waves, as indicated by Eq. (2). Thus, this model property has some limitations on the above-mentioned comparative analyses.

a. Propagation of WN-2 waves on the monopolar vortex

Figure 10 compares the propagation characteristics of the three classes of waves, based on the linear superimposition and numerical integration approaches. Eight eigenmodes from each wave class are selected with their eigenfrequency indices b and wave characteristics determined from the knowledge of Figs. 5 and 7, respectively; their summations for each wave class at $t = 0$ are then defined as the initial (composite) perturbations. Note that for each wave class the coefficient C_b should be set to be either 1 for selected eigenmodes or 0 for unselected eigenmodes when the summations in Eq. (10) are executed at $t = 0$ or any subsequent time using the linear superimposition method.

We see that the initial composite perturbations represent well the WN-2 characteristics of IGWs (Figs. 10a,j), VRWs (Figs. 10b,k), and VRIGWs (Figs. 10c,l) in terms of rotation and divergence, and the mass–wind relation;

their radial structures and wave amplitudes [as well as vorticity and divergence (not shown)] are similar to those associated with single waves shown in Fig. 7. Moreover, we can still see a wide radial range of the IGWs and VRIGWs activity (i.e., greater than 200 km) but a limited radial range of the VRWs activity (i.e., less than 50 km), as determined by their r_c (cf. Figs. 10 and 7).

Because of its fast azimuthal propagation, the IGWs from both approaches develop lengthy spiral bands after 60 min (Figs. 10d,g). By comparison, the VRWs exhibit slow clockwise propagation within r_c, only having slight shape changes even after 120 min (Figs. 10e,h). Large cross-isobaric (divergent) and nearly isobaric (rotational) flows can be clearly seen from the IGWs and VRWs, respectively. However, numerical integrations tend to inevitably produce slightly more rotational and divergent components associated with the respective IGWs and VRWs than those from the linear superimposition, as expected from the earlier discussion. The modeled flows are also stronger (weaker) in the central area for the IGWs (VRWs) than those superimposed (cf. Figs. 10d,e and 10g,h) because of the influences of the other waves, similarly for the faster clockwise movements of the VRWs. So, strictly speaking, the waves shown in Figs. 10g and 10h are not pure ones.

The right column of Fig. 10 displays the mixed-wave characteristics of the IGWs and VRWs with complicated mass and wind relations. That is, the initial perturbations (Fig. 10c) exhibit rotational (divergent) characteristics of VRWs (IGWs) within $r = 50$ km (outside roughly $r_c = 130$ km), with their structures similar to those shown in Fig. 10b (Fig. 10a). Between the two radii, we see the coexistence of both rotation and divergence with 45° phase shift, as indicated by local flow vectors with respect to isobars, which are the exact characteristics of mixed VRIGWs. At $t = 120$ min, Fig. 10f shows well-structured spiral bands within $r = 200$ km of the linear superimposed mixed VRIGWs, like the IGWs, but with the major highs and lows trapped within $r_c = 130$ km, like the VRWs (Fig. 10f). Of importance is that like the equatorial mixed Rossby–gravity waves, the mixed VRIGWs are characterized by near-isobaric circulations associated with the highs and lows, but cross-isobaric flows outside r_c. Of further importance is that their height and wind perturbations attenuate at rates (Figs. 10c,f) that are much slower than those of the IGWs (Figs. 10a,d) and VRWs (Figs. 10b,e), implying that such quasi-balanced wave properties may have more significant impact than the other waves on the maintenance of rainbands in TCs.

By comparison, numerical integrations produce more pronounced distortions of the mixed VRIGWs than the VRWs (Figs. 10h,i). They can be seen from the height
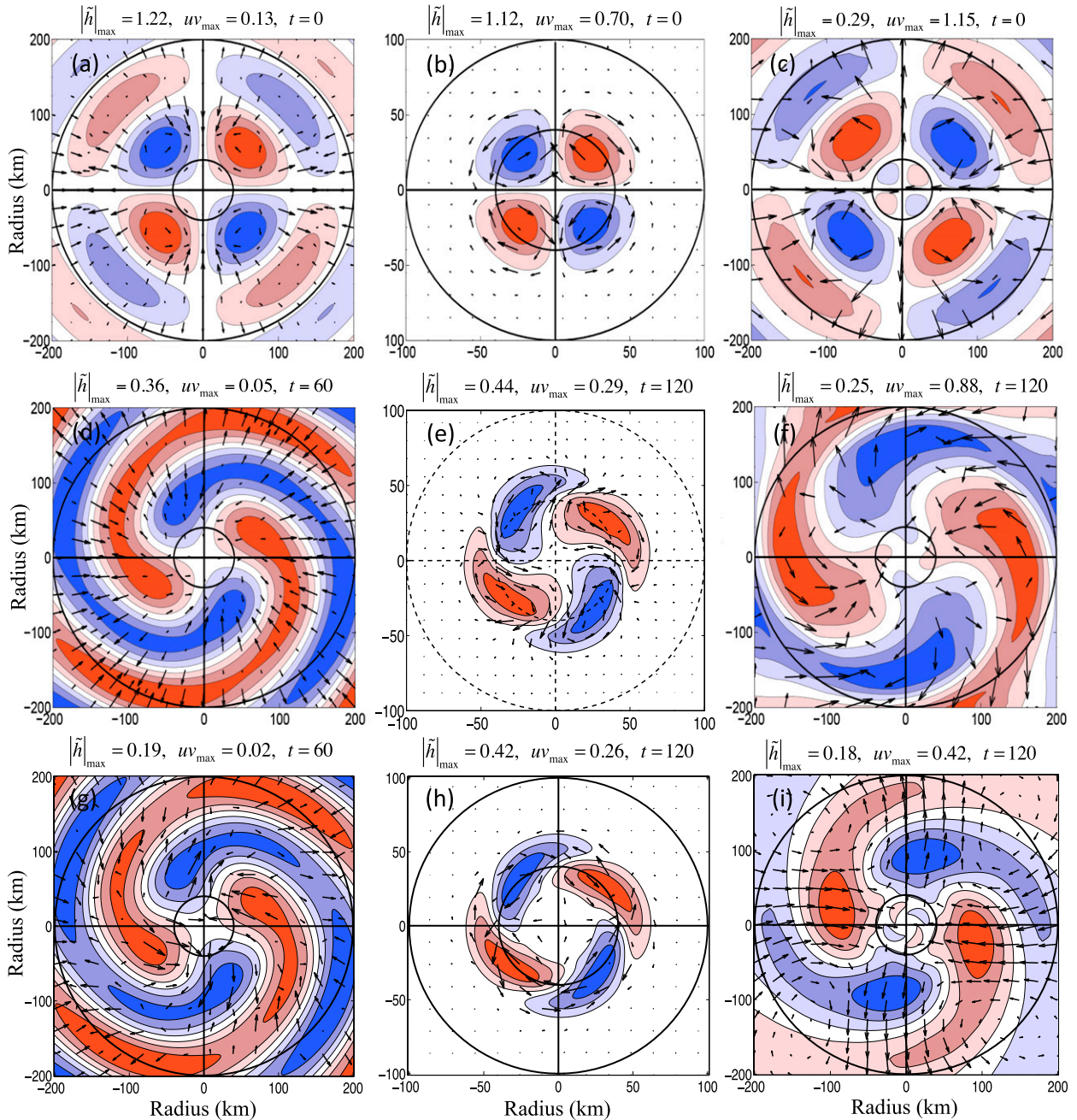
FIG. 10. The evolution of perturbation height (m; shaded, red is positive and blue is negative) and horizontal flow vectors (m s^{-1}) for (a),(d),(g) WN-2 IGWs, (b),(e),(h) VRWs, and (c),(f),(i) mixed VRIGWs on the monopolar vortex given in Fig. 1 at (top) $t = 0$, and $t = 60$ min for the IGWs and $t = 120$ min for the VRWs and mixed VRIGWs obtained from (middle) the linear-superimposed waves and (bottom) the SWVPAS model. Eight eigenvectors are selected from Eq. (10) with the eigenfrequency indices of $b = 3936, 3938, 3940, 3942, 3943, 3945,$ 3947, 3949 for the IGWs, $b = 4031, 4033, 4038, 4040, 4045, 4048, 4055, 4051$ for the VRWs, and $b = 4156, 4164, 4175, 4180, 4193, 4208, 4235,$ 4242 for the mixed VRIGWs, corresponding to the eigenfrequencies of $(5.60, 5.43, 5.26, 5.09, 4.92, 4.75, 4.58, 4.41) \times 10^{-3}$ s^{-1}, $(1.65, 1.59,$ $1.54, 1.46, 1.36, 1.32, 1.25, 1.19) \times 10^{-3}$ s^{-1}, and $(3.25, 2.98, 2.68, 2.55, 2.24, 1.96, 1.56, 1.47) \times 10^{-4}$ s^{-1}, respectively. The wave structures are displayed within the radial range of 200 km for the IGWs and mixed VRIGWs but only 100 km for the VRWs. The inner circle has a radius of 50 km for the IGWs and mixed VRIGWs and 40 km (where the RMζ is located) for the VRWs. For each variable α, seven color scales as determined by $(\alpha_{max} - \alpha_{min})/7$ are used, where α_{max} and α_{min} are the maximum and minimum value of α, respectively.

and wind perturbations that are completely out of phase outside $r = 100$ km, with more cross-isobaric components over wide regions. As will be shown next, these features are transient during this adjustment period in which all the three classes of waves interact.

b. Propagation of WN-2 waves on the hollow vortex

A different set of eight eigenmodes is also selected for each wave class propagating on the hollow vortex in order to see individually different WN-2 wave characteristics from those associated with the monopolar vortex. It is necessary to select such a different set of eigenmodes, although it is still close to the one used in Fig. 10, because the distribution of the wave classes differ under different basic states, as shown in Fig. 5. Indeed, Figs. 11a–c exhibit similar composite perturbation structures to those shown in Figs. 10a–c at $t = 0$, if viewed within $r = 70$ km, except for nearly vanishing flows in the central region and the elongated h' pattern associated with the VRWs (cf. Figs. 11b and 10b). Moreover, to facilitate comparisons to the analytical solutions of ZZL in which the critical radius is absent after assuming nonzero intrinsic frequency (i.e., $\overline{\omega} = \tilde{\omega} - n\overline{\Omega}_0 \neq 0$), we have eliminated the singularity in the vicinity of r_c (50 km for the VRWs, and 300 km for the VRIGWs, as shown in Figs. 8b and 8d) by performing nine-point smoother. As a result, the initial composite-wave structures resemble quite well the analytical solutions shown in Fig. 9 of ZZL, albeit with some differences in detailed structures.

Like in the monopolar vortex, the linear superimposition also produces well-structured spiral bands in the hollow vortex for the IGWs at $t = 60$ min, and the other two waves $t = 120$ min. However, because of the reduced vortex intensity, their azimuthal propagations are slower than those in ZZL (cf. Figs. 9b,e,h in ZZL and Figs. 11d–f herein). Of significance is that after 120 min, the mixed waves develop more rotational characteristics inside the RMW, like the VRWs, because of the presence of strong inertial stability, but more divergent characteristics outside, like the IGWs (Fig. 11f). This can also be seen from the distribution of S^2 in Fig. 9 showing a balanced regime within $r = 50$ km (i.e., $S^2 < 1$), and unbalanced regimes beyond the RMW (i.e., $S^2 > 1$). This inseparable property is unique for mixed VRIGWs compared to IGWs. Despite the presence of the IGW characteristics, the peak h' amplitude of the mixed waves only attenuates 40% after 120 min, as compared to the 50% reduction of the VRWs.

Because of the unstable basic state of the hollow vortex, as also indicated by their h' amplitudes (cf. Figs. 11g–i and 11d–f), numerical integrations produce more significant distortions of all the three waves than those

associated with the monopolar vortex (cf. Figs. 11g–i and 10g–i), such as the radially coupled h' within $r = 40$ km for the IGWs, and the more circular motions with an opposite phase relationship between the wind and height perturbations for both the VRWs and VRIGWs. In particular, the numerically integrated waves exhibit little spiral structures for the lower-frequency waves (Figs. 11h,i), as compared to the results of ZZL and linear superimposition. These waves also show sharp intensification within the RMW (Figs. 11h,i) and outward dispersion of the VRIGWs outside the RMW (Fig. 11i). In this regard, NMG indicated the growth of VRWs on a hollow vortex from numerical integrations using SWVPAS. Nevertheless, the long period of integrations shows little unbalanced flow, but balanced circulation of VRWs within the RMW (Figs. 11j–l); this is clearly determined by the SWVPAS dynamics, since the influences of the initial conditions decrease with time.

5. Summary and conclusions

In this study, the SWVPAS numerical model is used as a tool to study the matrix eigenvalue problems associated with the propagations of IGWs, VRWs, and mixed VRIGWs on the monopolar and hollow vortices. An eigenfrequency analysis indicates that as long as $\overline{\Omega}_{\max} < \overline{\Omega}_l = c_0\overline{m}\sqrt{n^2 + 3}$, the low-frequency VRWs and the two oppositely propagating high-frequency IGWs are well separated, which correspond to a continuous spectrum between 0 and $n\overline{\Omega}_{\max}$ and two discrete spectral regions on both sides, respectively. However, as the vortices reach hurricane intensity, part of the high-frequency IGWs will be "red shifted" to the continuous spectral region. On the other hand, the low-frequency VRWs on the hollow vortex will be "violet shifted" into the discrete spectral region because of a sign change in the radial gradient of the mean absolute vorticity. Thus, the mixed VRIGWs emerge from the frequency shifts in the presence of intense rotational flows.

An eigenfunctional analysis reveals three distinct radial wave structures associated with three classes of waves in the SWVPAS model: (i) IGWs exhibit more wavelike structures with dominant divergent flows, and their $\tilde{h}$ and $\tilde{\zeta}$ fields in the core region are in phase, with unbalanced characteristics. (ii) VRWs have little radial wavelike structures, but with dominant vortical flows, and their $\tilde{h}$ and $\tilde{\zeta}$ fields are antiphased, implying their balanced nature. In addition, the waves have a critical radius in the core region at which the inflexion points of the radial $\tilde{h}$ and $\tilde{u}$ profiles are located and $\overline{v}$ becomes discontinuous. (iii) Mixed VRIGWs, possessing both the IGW and VRW characteristics at higher WNs, exhibit both vortical and divergent flows at a similar order of
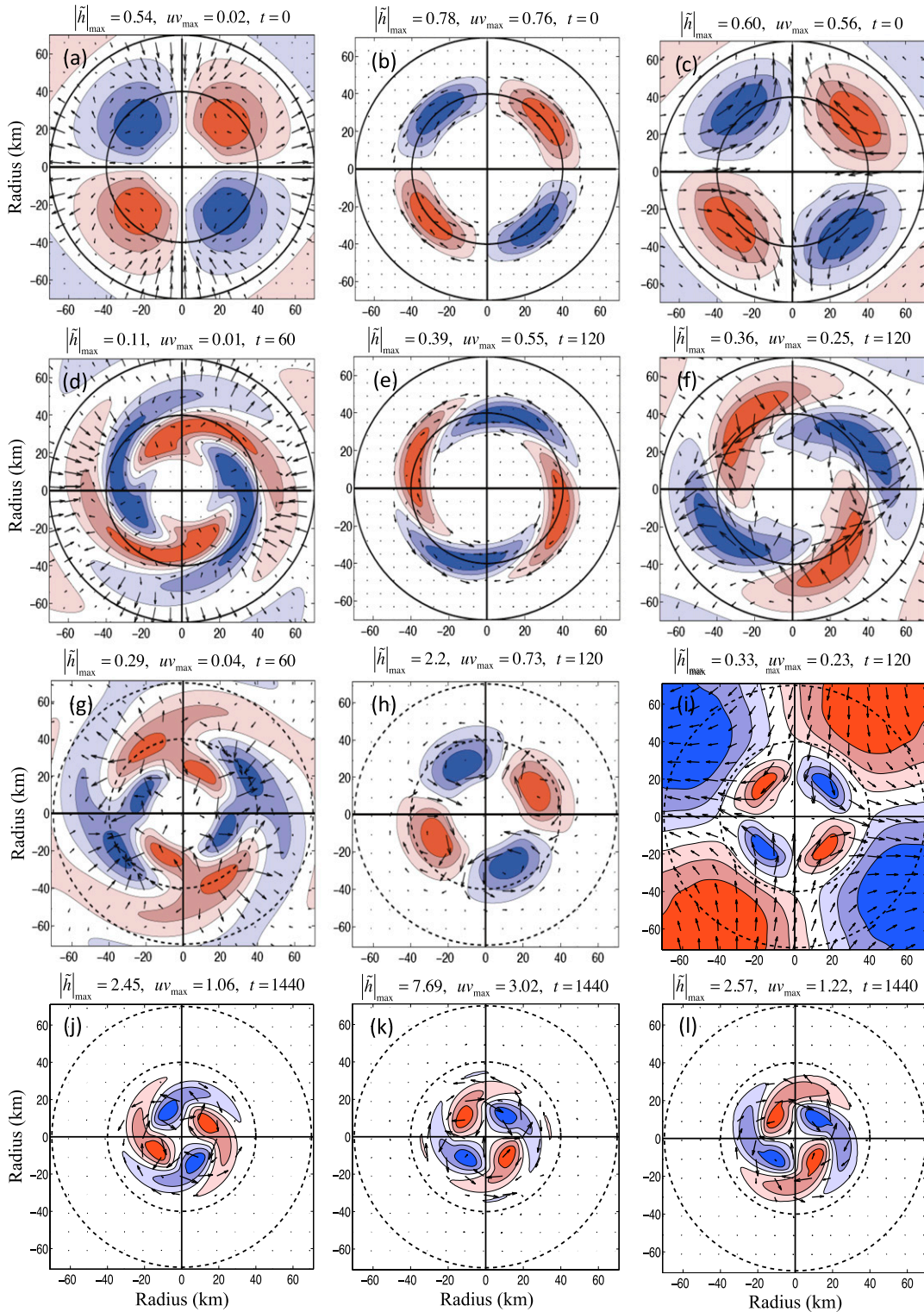
FIG. 11. As in Fig. 10, but for (d)–(f) the linear-superimposed waves and (g)–(i) the SWVPAS model at $t =$ 60 (120) min for (j)–(l) the IGWs (VRWs and mixed VRIGWs) and $t = 1440$ min with eigenfrequencies of (left) (5.3, 5.2, 5.0, 4.9, 4.6, 4.3, 3.9, 3.7) $\times 10^{-3}$ s^{-1} for IGWs, (middle) (1.61, 1.57, 1.56, 1.53, 1.52, 1.46, 1.45, 1.40) $\times 10^{-3}$ s^{-1} for VRWs, and (right) (2.65, 2.62, 2.60, 2.53, 2.51, 2.46, 2.37, 2.34) $\times 10^{-4}$ s^{-1} for mixed VRIGWs on the hollow vortex given in Fig. 1. The wave structures are displayed within the radial range of 70 km given by the outer circle (i.e., as in Fig. 9 of ZZL). The inner circles have a radius of 40 km.

magnitude. They also have critical radii, but in the outer regions. Moreover, their $\tilde{h}$ and $\tilde{\zeta}$ fields are out of phase in the core region, like VRWs, while changing to an in-phase relationship in the outer region, like IGWs, implying different geostrophic adjustment mechanisms between the inner and outer regions. These mixed-wave characteristics are more pronounced in hollow vortices than those in monopolar vortices because of the development of inflexion instability in the former.

Eight eigenmodes for each wave class are selected and linearly superimposed in time to gain insight into different propagation characteristics of the three wave classes on the monopolar and hollow vortices. Results show that cross-isobaric flows and isobaric flows associated with the IGW and VRWs, respectively, as expected, whereas the VRIGWs exhibit more balanced flows, like the VRWs, inside the RMW, but more unbalanced characteristics outside, like the IGWs. Moreover, the IGWs propagate rapidly outward as spiral bands, in significant contrast to the slow propagation of the VRWs and VRIGWs. The latter two waves tend to be trapped within their critical radii. On the other hand, the IGWs weaken rapidly with time, whereas both the VRWs and VRIGWs show slow reductions in amplitude. This indicates the potential importance of the VRWs and VRIGWs in maintaining spiral rainbands and organizing deep convection in the eyewall.

It is shown that numerical solutions of pure classes of the composite waves on the hollow vortex are generally similar to the analytical results of ZZL, except for some differences in small-scale details owing to the use of Doppler-shifted frequencies and the existence of r_c. Thus, we may conclude that VRIGWs, at least at WN 2, containing both intense vortical and divergent flows, should be common in TCs, especially in intense hurricanes. In a forthcoming study, we will examine the structural evolution of these waves using real-data-simulated hurricane cases and investigate their roles in the formation of spiral rainbands and the eyewall replacement cycle.

APPENDIX

Frequency Separation between IGWs and VRWs

Starting from the dispersive relation of IGWs in the linearized shallow-water equations (ZZL),

$$\tilde{\omega}_G = n\overline{\Omega}_0 + \overline{\omega}_G = n\overline{\Omega}_0 \pm \sqrt{c_0^2 \overline{m}_0^2 - \overline{\eta}_0 \overline{\Omega}_0}, \quad \text{(A1)}$$

the IGWs frequency must satisfy $\tilde{\omega}_G > n\overline{\Omega}_{\max}$ or $\tilde{\omega}_G < 0$, which can be written in a general form,

$$\tilde{\omega}_G^2 > (n\overline{\Omega}_{\max})^2. \quad \text{(A2)}$$

We may have the following inequality after combining Eqs. (A1) and (A2),

$$c_0^2 \overline{m}_0^2 - \overline{\eta}_0 \overline{\Omega}_0 > c_0^2 \overline{m}_0^2 - \overline{\eta}_{\max} \overline{\Omega}_{\max} > (n\overline{\Omega}_{\max})^2. \quad \text{(A3)}$$

By definition, we may assume $\overline{\eta}_{\max} > 3\overline{\Omega}_{\max}$, and then substitute it to Eq. (A3). This will give the threshold value of the basic-state angular velocity, $\overline{\Omega}_l = c_0 \overline{m} \sqrt{n^2 + 3}$, which can be used to distinguish the high-frequency IGWs from the low-frequency VRWs (see text).

REFERENCES

Black, M. L., and H. E. Willoughby, 1992: The concentric eyewall cycle of Hurricane Gilbert. *Mon. Wea. Rev.,* **120,** 947–957, doi:10.1175/1520-0493(1992)120<0947:TCECOH>2.0.CO;2.

Chen, H., D.-L. Zhang, J. Carton, and R. Atlas, 2011: On the rapid intensification of Hurricane Wilma (2005). Part I: Model prediction and structural changes. *Wea. Forecasting,* **26,** 885–901, doi:10.1175/WAF-D-11-00001.1.

Davis, C. A., and M. L. Weisman, 1994: Balanced dynamics of mesoscale vortices produced in simulated convective systems. *J. Atmos. Sci.,* **51,** 2005–2030, doi:10.1175/1520-0469(1994)051<2005:BDOMVP>2.0.CO;2.

Eidelman, Y., V. D. Milman, and A. Tsolomitis, 2004: *Functional Analysis: An Introduction.* American Mathematical Society, 75 pp.

Elsberry, R. L., W. M. Frank, G. J. Holland, J. D. Jarrell, and R. L. Southern, 1987: *A Global View of Tropical Cyclones.* University of Chicago Press, 185 pp.

Flatau, M., and D. E. Stevens, 1989: Barotropic and inertial instabilities in the hurricane outflow layer. *Geophys. Astrophys. Fluid Dyn.,* **47,** 1–18, doi:10.1080/03091928908221814.

Guinn, T. A., and W. H. Schubert, 1993: Hurricane spiral bands. *J. Atmos. Sci.,* **50,** 3380–3403, doi:10.1175/1520-0469(1993)050<3380:HSB>2.0.CO;2.

Hogsett, W., and D.-L. Zhang, 2009: Numerical simulation of Hurricane Bonnie (1998). Part I: Energetics. *J. Atmos. Sci.,* **66,** 2678–2696, doi:10.1175/2009JAS3087.1.

Holton, J. R., 2004: *An Introduction to Dynamic Meteorology.* 4th ed. Elsevier Academic, 535 pp.

Jorgensen, D. P., 1984: Mesoscale and convective-scale characteristics of mature hurricanes. Part I: Inner core structure of

hurricane Allen (1980). *J. Atmos. Sci.,* **41,** 1287–1311, doi:10.1175/1520-0469(1984)041<1287:MACSCO>2.0.CO;2.

Kurihara, Y., 1976: On the development of spiral bands in a tropical cyclone. *J. Atmos. Sci.,* **33,** 940–958, doi:10.1175/1520-0469(1976)033<0940:OTDOSB>2.0.CO;2.

Lee, W.-C., and M. M. Bell, 2007: Rapid intensification, eyewall contraction, and breakdown of hurricane Charley (2004) near landfall. *Geophys. Res. Lett.,* **34,** L02802, doi:10.1029/2006GL027889.

Liu, Y., D.-L. Zhang, and M. K. Yau, 1997: A multiscale numerical study of Hurricane Andrew (1992). Part I: Explicit simulation and verification. *Mon. Wea. Rev.,* **125,** 3073–3093, doi:10.1175/1520-0493(1997)125<3073:AMNSOH>2.0.CO;2.

——, ——, and ——, 1999: A multiscale numerical study of Hurricane Andrew (1992). Part II: Kinematics and inner-core structures. *Mon. Wea. Rev.,* **127,** 2597–2616, doi:10.1175/1520-0493(1999)127<2597:AMNSOH>2.0.CO;2.

Macdonald, N. J., 1968: The evidence for the existence of Rossby-like waves in the hurricane vortex. *Tellus,* **20,** 138–150, doi:10.1111/j.2153-3490.1968.tb00358.x.

Marks, F. D., Jr., and R. A. Houze Jr., 1987: Inner core structure of Hurricane Alicia from airborne Doppler radar observations. *J. Atmos. Sci.,* **44,** 1296–1317, doi:10.1175/1520-0469(1987)044<1296:ICSOHA>2.0.CO;2.

Matsuno, T., 1966: Quasi-geostrophic motions in the equatorial area. *J. Meteor. Soc. Japan,* **44,** 25–43.

Montgomery, M. T., and R. J. Kallenbach, 1997: A theory for vortex Rossby waves and its application to spiral bands and intensity changes in hurricanes. *Quart. J. Roy. Meteor. Soc.,* **123,** 435–465, doi:10.1002/qj.49712353810.

——, and C. Lu, 1997: Free waves on barotropic vortices. Part I: Eigenmode structure. *J. Atmos. Sci.,* **54,** 1868–1885, doi:10.1175/1520-0469(1997)054<1868:FWOBVP>2.0.CO;2.

Nolan, D. S., and M. T. Montgomery, 2002: Nonhydrostatic, three-dimensional perturbations to balanced, TC-like vortices. Part I: Linearized formulation, stability, and evolution. *J. Atmos. Sci.,* **59,** 2989–3020, doi:10.1175/1520-0469(2002)059<2989:NTDPTB>2.0.CO;2.

——, ——, and L. D. Grasso, 2001: The wavenumber-one instability and trochoidal motion of TC-like vortices. *J. Atmos. Sci.,* **58,** 3243–3270, doi:10.1175/1520-0469(2001)058<3243:TWOIAT>2.0.CO;2.

Pedlosky, J., 2003: *Waves in the Ocean and Atmosphere: Introduction to Wave Dynamics.* Springer-Verlag, 260 pp.

Schecter, D. A., and M. T. Montgomery, 2004: Damping and pumping of a vortex Rossby wave in a monotonic cyclones: Critical layer stirring versus inertia-buoyancy wave emission. *Phys. Fluids,* **16,** 1334–1348, doi:10.1063/1.1651485.

Schubert, W. H., M. T. Montgomery, R. K. Taft, T. A. Guinn, S. R. Fulton, J. P. Kossin, and J. P. Edwards, 1999: Polygonal eyewalls, asymmetric eye contraction, and potential vorticity mixing in hurricanes. *J. Atmos. Sci.,* **56,** 1197–1223, doi:10.1175/1520-0469(1999)056<1197:PEAECA>2.0.CO;2.

Wang, X., and D.-L. Zhang, 2003: Potential vorticity diagnosis of a simulated hurricane. Part I: Formulation and quasi-balanced flow. *J. Atmos. Sci.,* **60,** 1593–1607, doi:10.1175/2999.1.

Wang, Y., 2001: An explicit simulation of tropical cyclones with a triply nested movable mesh primitive equation model: TCM3. Part I: Model description and control experiment. *Mon. Wea. Rev.,* **129,** 1370–1394, doi:10.1175/1520-0493(2001)129<1370:AESOTC>2.0.CO;2.

——, 2002: Vortex Rossby waves in a numerically simulated tropical cyclone. Part I: Overall structure, potential vorticity, and kinetic energy budgets. *J. Atmos. Sci.,* **59,** 1213–1238, doi:10.1175/1520-0469(2002)059<1213:VRWIAN>2.0.CO;2.

Willoughby, H. E., 1978: A possible mechanism for the formation of hurricane rainbands. *J. Atmos. Sci.,* **35,** 838–848, doi:10.1175/1520-0469(1978)035<0838:APMFTF>2.0.CO;2.

——, J. A. Clos, and M. G. Shoreibah, 1982: Concentric eye walls, secondary wind maxima, and the evolution of the hurricane vortex. *J. Atmos. Sci.,* **39,** 395–411, doi:10.1175/1520-0469(1982)039<0395:CEWSWM>2.0.CO;2.

Zeng, Q.-C., R.-F. Li, and M. Zhang, 1990: The spectrum and eigenfunction in the two-dimensional compressible rotating flows. *Sci. Atmos. Sin.,* **14,** 129–142.

Zhang, D.-L., and C. Q. Kieu, 2006: Potential vorticity diagnosis of a simulated hurricane. Part II: Quasi-balanced contributions to forced secondary circulations. *J. Atmos. Sci.,* **63,** 2898–2914, doi:10.1175/JAS3790.1.

Zhong, W., H.-C. Lu, and D.-L. Zhang, 2008: The diagnoses of quasi-balanced flows in asymmetric intense hurricane. *Chin. J. Geophys.,* **51,** 468–479, doi:10.1002/cjg2.1238.

——, D.-L. Zhang, and H.-C. Lu, 2009: A theory for mixed vortex Rossby–gravity waves in tropical cyclones. *J. Atmos. Sci.,* **66,** 3366–3381, doi:10.1175/2009JAS3060.1.

——, H.-C. Lu, and D.-L. Zhang, 2010: Mesoscale barotropic instability of vortex Rossby waves in tropical cyclones. *Adv. Atmos. Sci.,* **27,** 243–252, doi:10.1007/s00376-009-8183-7.